Noname manuscript No.
(will be inserted by the editor)

Motion-Aware Stroke Volume Quantification in 4D PC-MRI Data of the Human Aorta

Benjamin Köhler · Uta Preim · Matthias Grothoff · Matthias Gutberlet · Katharina Fischbach · Bernhard Preim

Received: date / Accepted: date

Abstract *Purpose*: 4D PC-MRI enables the non-invasive measurement of time-resolved, three-dimensional blood flow data that allow quantification of the hemodynamics. Stroke volumes are essential to assess the cardiac function and evolution of different cardiovascular diseases. The calculation depends on the wall position and vessel orientation, which both change during the cardiac cycle due to the heart muscle contraction and the pumped blood. However, current systems for the quantitative 4D PC-MRI data analysis neglect the dynamic character and instead employ a static 3D vessel approximation. We quantify differences between stroke volumes in the aorta obtained with and without consideration of its dynamics.

Methods: We describe a method that uses the approximating 3D segmentation to automatically initialize segmentation algorithms that require regions inside and outside the vessel for each temporal position. This enables the use of graph cuts to obtain 4D segmentations, extract vessel surfaces including centerlines for each temporal position and derive motion information. The stroke volume quantification is compared using measuring planes in static (3D) vessels, planes with fixed angulation inside dynamic vessels (this corresponds to the common 2D PC-MRI) and moving planes inside dynamic vessels.

Results: Seven datasets with different pathologies such as aneurysms and coarctations were evaluated in close collaboration with radiologists. Compared to the experts' manual stroke volume estimations, motion-aware quantification performs, on average, 1.57% better than calculations without motion consideration. The mean difference between stroke volumes obtained with the different methods is 7.82%. Automatically obtained 4D segmentations overlap by 85.75% with manually generated ones.

Conclusions: Incorporating motion information in the stroke volume quantification yields slight but not statistically significant improvements. The presented method is feasible for the clinical routine, since computation times are low and essential parts run fully automatically. The 4D segmentations can be used for other algorithms as well. The simultaneous visualization and quantification may support the understanding and interpretation of cardiac blood flow.

Keywords 4D PC-MRI · CMR · Stroke Volume · Motion · Quantification · 4D Segmentation · Graph Cut

Benjamin Köhler · Bernhard Preim
Otto-von-Guericke University, Magdeburg, Germany
Department of Simulation and Graphics
E-mail: ben.koehler@isg.cs.uni-magdeburg.de

Uta Preim
Municipal Hospital, Magdeburg, Germany
Department of Diagnostic Radiology

Matthias Grothoff · Matthias Gutberlet
Heart Center, Leipzig, Germany
Department of Diagnostics and Interventional Radiology

Katharina Fischbach
University Hospital, Magdeburg, Germany
Department of Radiology and Nuclear Medicine

1 Introduction

Four-dimensional phase-contrast magnetic resonance imaging (4D PC-MRI) gained increasing importance in the last decade. It is a non-invasive image modality that allows qualitative and quantitative investigation of intravascular hemodynamics. Stroke volumes – the amount of pumped blood per heartbeat – help to assess the cardiac function and monitor progression of diseases such as bicuspid aortic valves and heart insufficiencies. Static 3D approximations of the dynamic vessel wall are widely used to calculate this measure. There is a trade-off between easier, faster preprocessing and accurate information about the heart's cyclic movement.

Techniques with an enhanced level of automation could overcome this issue by speeding up data processing. However, the accurate definition of intravascular hemodynamics requires the determination of the time-dependent wall position, wall orientation and vessel diameter. Approaches that neglect these components are error-prone.

The segmentation of time-varying cardiac image data was aimed at by several research groups. Algorithms such as graph cuts only require the specification of areas inside and outside the target structure, which is convenient for physicians since it exploits their anatomical expert knowledge. Based on heuristics that were derived from discussions with collaborating radiologists, we automatically initialize a 3D graph cut for each temporal position of the dataset and obtain a time-dependent binary mask of the aorta. A mesh model is described that contains motion information as vectorial displacement list per vertex. Displacement vectors are projections from a static vessel surface approximation onto the meshes of each time step. The latter were extracted from the 4D segmentation. This facilitates postprocessing of the movement information. We incorporate the vessel dynamics in a motion-aware stroke volume quantification and investigate the reliability of the conventional quantification using static vessels by examining deviations.

Section 2 describes related work w.r.t. qualitative and quantitative 4D PC-MRI data analysis and time-dependent cardiac segmentation approaches. Section 3 continues with details about selected cardiac diseases, data acquisition and preprocessing. The 4D segmentation, motion extraction and the adjusted stroke volume quantification are described in Section 4. Section 5 examines differences to static vessel quantification using various patient and healthy volunteer datasets. Our work is summarized in Section 6.

2 Related Work

4D PC-MRI: Stankovic et al. [31] provide basic information about 4D PC-MRI. It has the potential to become the leading image modality to assess cardiac hemodynamics since it allows a more flexible data analysis than its 2D counterpart. Calkoen et al. give an overview of recent applications [6].

Visual Analysis of 4D PC-MRI Data: The high complexity of the dynamic 3D flow data leads to heavy visual clutter. Various exploration approaches and expressive visualizations were introduced that facilitate better insight. Examples are speed lines by van Pelt et al. [25], further illustrative techniques by Born et al. [4] and the FlowLens [12] as well as ghosted viewing of the vessel front by Gasteiger et al. [13]. Preim et al. [28] describe methods tailored for the visual exploration of simulated and measured blood flow data. Line predicates are a threshold-based filtering technique for integral lines such as pathlines, which are commonly used to visualize blood flow. Line predicates were used by Born et al. [5] and Köhler et al. [18] to extract qualitative flow features such as vortices. Carnecky et al. [7] provide a special flow data preprocessing to improve noise robustness of the employed λ_2 vortex criterion. Hennemuth et al. [14] describe a pipeline for interactive 4D PC-MRI data processing and exploration.

Quantification in 4D PC-MRI Data: The quantification of stroke volumes allows an assessment of the cardiac function. Hope et al. [15] give an overview of further important measures such as pulse wave velocities. Van Ooij et al. [24] and Potters et al. [27] describe a method to determine vectorial wall shear stress, which is associated with vessel dilation, in measured data. The comparison with computational fluid dynamics (CFD) simulations showed a good correspondence of wall shear stress directions and peak location. Yet, absolute values are error-prone due to low spatial resolutions and high sensitivity to the exact wall position. Roldán-Alzate et al. [29] investigated thromboembolic pulmonary hypertension in a canine model. Francois et al. [11] found significant alterations in the pulmonary artery and right ventricle of tetralogy of Fallot patients.

4D Heart Segmentation and Visualization: Graph cuts were used to obtain spatio-temporal segmentations of the heart [8,20,21]. Other groups used level sets [37] or deformable models [1] for this purpose. GPU-accelerated time-varying direct volume rendering was used to display measured anatomical data [33,36]. Cine MRI is another common technique where a series of slice images throughout the cardiac cycle is acquired, which are then presented as movie.

3 Medical Background

4D PC-MRI data represent the blood flow dynamics throughout the cardiac cycle. During systole, oxygenated blood from the left ventricle is pumped through the aortic valve into the aorta (systemic circulation). Deoxygenated blood is pumped from the right ventricle through the pulmonary valve into the pulmonary artery (pulmonary circulation). During diastole, the valves are closed to prevent blood from flowing back.

3.1 Cardiovascular Vortex Flow

Flow in the great vessels is typically laminar with the highest velocities in the center. In the following, we explain selected valvular and vascular pathologies that promote the formation of vortex flow. Köhler et al. [19] pointed out the high susceptibility of stroke volume quantification to such complex flow patterns.

Vascular Diameter Alterations: Slight dilations up to $1.5\times$ the original vessel diameter are called *ectasia*, above they are referred to as *aneurysm*. In contrast, *stenosis* / *coarctation* defines an abnormal narrowing. The altered ves-

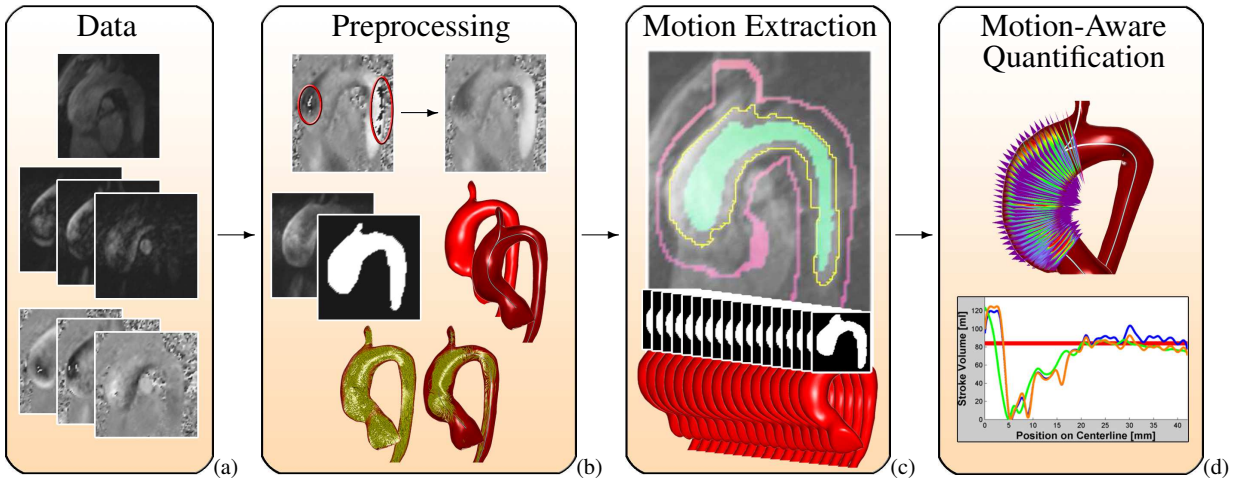

Fig. 1: (a) Anatomical images from averaged signal intensities, magnitude (undirected flow strength) and phase images (flow direction and strength) from a 4D PC-MRI sequence. (b) Artifact correction, temporal maximum intensity projection (TMIP) of the magnitude images, static vessel segmentation, initial surface reconstruction and centerline extraction, full flow integration and vortex extraction. (c) 4D segmentation and motion extraction. (d) Motion-aware stroke volume quantification and assessment of differences to results calculated in static vessels and using a 2D PC-MRI simulation.

sel shape promotes the formation of vortex flow in both cases.

Valve Pathologies: *Stenotic valves* are abnormally narrowed. *Insufficient valves* do not close properly and cause an abnormal amount of diastolic back flow that negatively affects the cardiac function. If the aortic valve (AV) consists of only two instead of three leaflets, it is called a *bicuspidality (BAV)* – a setting that often leads to systolic vortex flow in the ascending aorta [16]. Valve replacements are invasive and should be performed only when a positive benefit-risk ratio is likely.

Tetralogy of Fallot: This congenital pathology is characterized by an *infundibular* and / or *stenotic pulmonary valve* and a *ventricular septal defect*. After correction of both within months after birth, *Fallot* patients are highly vulnerable to developing a *pulmonary insufficiency*.

3.2 Data Acquisition and Preprocessing

A 3 T Magnetom Verio (Siemens Healthcare, Erlangen, Germany) with a dedicated 32-channel cardiac coil was used for data acquisition. A 4D PC-MRI dataset consists of seven images. Three phase (also: gradient, velocity) images describe the flow direction and strength for each patient-oriented xyz dimension. Three magnitude images describe the undirected flow strength and are less prone to uncorrelated noise. One anatomy image is reconstructed from averaged signal intensities. Each image has the same spatio-temporal resolution. The imaging parameters were as follows: slice thickness 3.5 mm, flip angle 15^o, field of view 340 mm, echo time 3.2 ms, repetition time 6.1 ms, temporal resolution 49 ms, sampling bandwidth 491 Hz/pixel, reconstructed phases 10-20, one acquisition. The maximum expected velocity (V_{ENC}) was set to 1.5 m/s per dimension. A sagittal oblique 3D slab was positioned to include the aorta. Heart and wall motion artifacts were minimized using prospective ECG gating. The spatial in-plane resolution is 1.77 mm$\times$1.77 mm in a 132$\times$192 grid with 15-23 slices. Isotropic resolution was not used, since it would have lengthened the already 20 min long acquisitions. The same yields for respiratory control. Eddy current (also: velocity offset) correction [34] and phase unwrapping [9] were applied to the phase images. Figure 1 depicts the pipeline.

Static Vessel Segmentation: A temporal maximum intensity projection (TMIP) of the magnitude images yields a high contrast 3D image [25]. Regions with high velocity magnitudes in at least one time point are emphasized. Since flow in the aorta is fast, it is clearly visible in the TMIP image. A graph cut with a 26-neighborhood per voxel (GridCut) is employed to obtain a segmentation of the aorta as static approximation. Edge weights are set to $exp(-\alpha \cdot ||\nabla I||^2)$. Gradients in the TMIP with $[0,1]$-scaled intensities I are calculated via finite differences. The higher the tolerance parameter α is, the larger the segmented region becomes. $\alpha = 1000$ is used as an experimentally determined default value. Depending on the TMIP quality, the user has to specify fewer or more regions inside and outside the vessel as graph cut input. For noise reduction, 3$\times$3$\times$3 morphological closing and opening is applied to the resulting 3D segmentation.

Initial Surface Reconstruction: Marching cubes is employed to extract a triangular vessel surface from the segmentation. The aorta's surface is not complex and wall motion is mainly pulsatile. Thus, few triangles are sufficient to represent its shape. To minimize discontinuities in of the surface, the mesh is smoothed using a low-pass filter [32] (50 iterations, passband $= 0.1$) that is suitable for medical surface models [3] and reduced via quadric decimation [17] (topology preserving, target reduction $= 0.8$). The parameters are experimentally determined default values. Afterwards, the centerlines are extracted [2,26]. In our datasets, they produced 2771 triangles on average with a mean area of 10.43 ± 0.27 mm^2. This corresponds to approximately 4.9 mm edge length in equilateral triangles. For comparison, a voxel diagonal is 4.3 mm long.

Flow Calculation: The GPU is utilized to integrate the full set of pathlines [10] and to derive the λ_2-criterion that is required for the line predicate-based vortex extraction [18]. Velocity vectors $\mathbf{u} \in \mathbb{R}^3$ in the 4D flow field $\mathbb{V}$ at the spatio-temporal position $\mathbf{x} = (x,y,z,t)^{\mathrm{T}}$ are obtained using quadrilinear interpolation. The temporally adjacent vectors $\mathbf{u}_{\lfloor t \rfloor} = \mathbb{V}(x,y,z,\lfloor t \rfloor)$ and $\mathbf{u}_{\lceil t \rceil} = \mathbb{V}(x,y,z,\lceil t \rceil)$, both obtained via hardware-accelerated trilinear interpolation, are used to perform a last linear interpolation manually. Pathline visualization is enhanced with illuminated streamlines and halos [22] to improve spatial and depth perception. Particles with trails are shown during animation. A ghosted viewing [13] shows parts of the cut away vessel front.

4 Motion Extraction and Adjusted Stroke Volume Quantification

In the following, we describe the 4D segmentation of the aorta and the steps to obtain and postprocess movement information. After the adjustment of centerlines and measuring planes, the stroke volume quantification is adapted.

4.1 Stroke Volume Quantification in Static (3D) Vessels

The stroke volume (SV) is the amount of blood that passes a measuring plane over the aortic valve orthogonally during a heartbeat. This requires the time-dependent flow rate $fr(t)$. For a measuring plane P it is obtained as:

$$fr(t) = s_x \cdot s_y \cdot \mathbf{n} \cdot \sum_{x=0}^{g_x-1} \sum_{y=0}^{g_y-1} S_3(P(x,y)) \cdot \mathbb{V}(P(x,y),t)$$

$$\text{with} \quad S_3(P(x,y)) = \begin{cases} 1, & P(x,y) \text{ inside vessel} \\ 0, & \text{else} \end{cases} \qquad (1)$$

$$\text{and} \quad P(x,y) = \mathbf{c} + s_x \cdot \left(x - \frac{g_x}{2}\right) \cdot \mathbf{n}_x + s_y \cdot \left(y - \frac{g_y}{2}\right) \cdot \mathbf{n}_y$$

Based on [19], a measuring plane is characterized by a grid size $\mathbf{g} = (g_x, g_y)$ with 50×50 as default, a center position $\mathbf{c} \in \mathbb{R}^3$, a normal vector $\mathbf{n} \in \mathbb{R}^3$ that describes the plane's orientation, a scale $\mathbf{s} = (s_x, s_y)$ per grid element and two vectors $\mathbf{n}_x, \mathbf{n}_y$ that form a local orthonormal system with $\mathbf{n}$. The scale is determined so that the plane fits the diameter of the corresponding vessel section. $P(x,y) \in \mathbb{R}^3$ is a grid position transformed to world coordinates. The product $s_x \cdot s_y$ is the area per grid element. $\mathbb{V}(P(x,y),t)$ are velocity vectors in the flow field $\mathbb{V}$, which is given by the phase images from the 4D PC-MRI dataset. The SV results as integral of the periodic flow rate $fr(t)$.

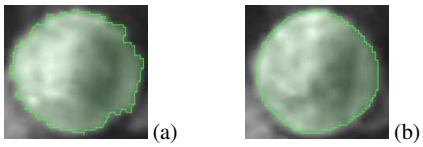

Fig. 2: Mask of an aorta's cross-section obtained from rasterization of (a) the 3D vessel segmentation and (b) the extracted corresponding triangular surface.

$S_3(P(x,y))$ describes the check whether or not a position is inside the vessel. When applied to each grid element of the measuring plane, it yields a 2D segmentation of the cross-section. The segmentation's resolution is given by the plane's grid size $\mathbf{g}$. $S_3(P(x,y))$ can be realized using the voxel-based 3D segmentation, which is rather coarse compared to the resolution of the plane's grid elements. However, it facilitates usage of the GPU, since it can be employed as 3D texture. A smoother result can be obtained by rasterizing the 3D mesh, as depicted in Figure 2. This is what we use for this work.

4.2 Four-Dimensional Vessel Segmentation

Performing a manual vessel segmentation in every temporal position is too time-consuming for the clinical routine. Therefore, we automatically determine regions inside and outside the aorta for each time step based on the 3D segmentation and employ this to initialize graph cuts. Other segmentation algorithms that require the same kind of input are also suitable. We perform one 3D graph cut for each time step in the 4D anatomical image.

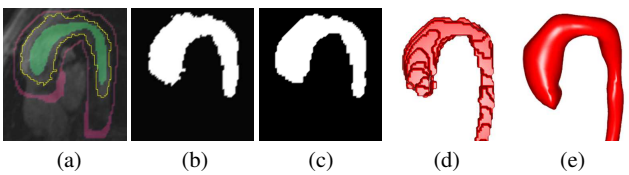

Fig. 3: Extraction procedure for each temporal position. (a) Automatic specification of regions inside (green) and outside the aorta (red) as graph cut initialization. (b) Resulting 3D segmentation. (c) Postprocessed segmentation. (d) Extracted triangular surface. (e) Postprocessed vessel mesh.

The 3D segmentation, based on the magnitude images' TMIP, represents blood-filled vessels during systole and therefore the maximum extent – like an upper boundary. Thus, we assume that voxels outside this segmentation are also outside the segmentation of each temporal position. A safety margin is incorporated to consider inaccuracies. We subtract a kernel size 5 from a kernel size 8 dilated segmentation to obtain a dilated vessel hull. This is about 1-2 cm away from the vessel surface for the data's spatial resolution of $1.77\times1.77\times3.5$ mm^3. We observed that a smaller margin does not improve the results of the employed graph cut. Based on discussions with radiologists, a second assumption is made that the vessel diameter does not shrink more than 50% during diastole. Hence, all voxels are specified as inside the vessel that are closer to the centerline than to the wall. The same initialization is used for all time steps and graph cuts are performed separately for each of them.

Image quality, in particular the signal-to-noise ratio, depends on the acquisition time. In patients with severe heart diseases, acquisitions need to be performed in limited time with a quality that is just sufficient for diagnosis. As a consequence, the graph cut tolerance parameter α is increased by a factor of ten. The resulting segmentations for each temporal position are postprocessed in the same manner as described in Section 3.2. The same applies to the extraction and postprocessing of the polygonal 3D meshes. Figure 3 depicts the process.

4.3 Dynamic (4D) Vessels

Displacement Vectors: We aim at extracting motion information that can be postprocessed in order to reduce noise. Until now, we obtained independent 3D meshes M_t for each of the T temporal positions $t = 0\dots T\text{-}1$ in the dataset. Unfortunately, the meshes may differ in their number of vertices and topology. Thus, a vertex' time-dependent position $\mathbf{v}_t^{\text{dspl}}$ cannot be derived implicitly. For the association of points on the surfaces with each other, a correspondence problem has to be solved.

A 4D mesh model requires a certain flexibility to capture pathologic vessel morphologies. We employ a 3D triangular surface mesh M with a constant topology as basis. It is the one extracted from the 3D segmentation that was performed on the magnitude images' TMIP. Every vertex $\mathbf{v} \in M$ stores

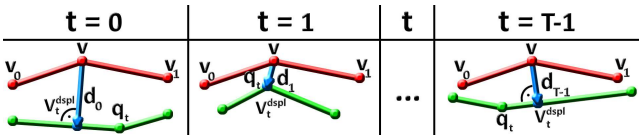

Fig. 4: The projection $\mathbf{v}_t^{\text{dspl}}$ of a base mesh vertex $\mathbf{v}$ (red) onto the one-ring neighborhood of the closest vertex $\mathbf{q}_t$ in the mesh M_t (green) of a temporal position t is determined to obtain the displacement vector $\mathbf{d}_t$ (blue) as $\mathbf{v}_t^{\text{dspl}} - \mathbf{v}$.

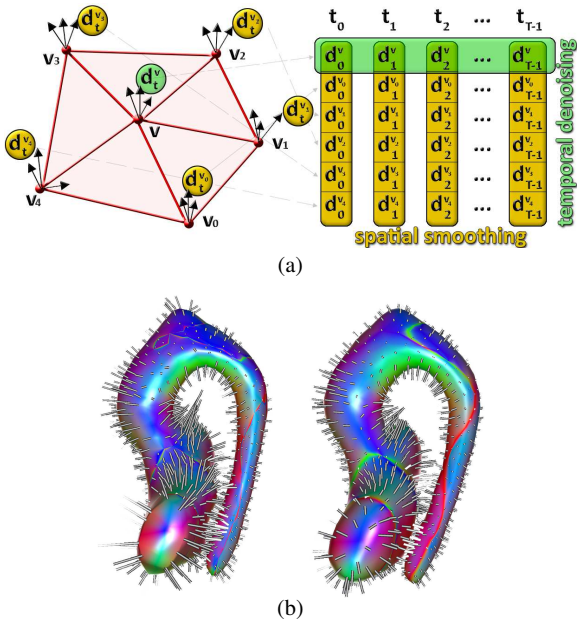

Fig. 5: (a) Displacement postprocessing. The spatial smoothing (orange) is a low-pass filter applied to the displacements $\{\mathbf{d}_t^{v}, \mathbf{d}_t^{v_i}\}$ of the one-ring neighborhood $\mathbf{v}_i$ of the mesh vertex $\mathbf{v}$ in each temporal position $t = 0\dots T\text{-}1$. The temporal denoising (green) smoothes the displacement list $\mathbf{d}_t^{v}$ of $\mathbf{v}$. (b) Displacement vectors (white lines) of one temporal position without (left) and with (right) noise reduction. The surface is colored according to the displacements.

a list of T 3D vectors $\mathbf{d}_t$, in the following referred to as displacement vectors. A vertex' position $\mathbf{v}_t^{\text{dspl}}$ at time t is $\mathbf{v}+\mathbf{d}_t$.

Displacements $\mathbf{v}_t^{\text{dspl}}$ are calculated as closest projection of a vertex $\mathbf{v} \in M$ onto M_t. To do so, the nearest vertex $\mathbf{q}_t \in M_t$ to $\mathbf{v}$ is determined. Then, $\mathbf{v}$ is projected onto each plane spanned by the triangles that $\mathbf{q}_t$ is part of. If a projection lies outside a triangle, the closest projection onto one of the triangle's edges is used as result. The displacement vector $\mathbf{d}_t$ results as $\mathbf{v}_t^{\text{dspl}} - \mathbf{v}$, see Figure 4.

Displacement Postprocessing: For noise reduction of the displacement vector lists, two postprocessing steps are applied, as depicted in Figure 5:

- The **spatial smoothing** aligns displacement vectors in a vertex' one-ring neighborhood in each temporal position separately. The same low-pass filter [32] as for the mesh smoothing is used for this purpose.
- The **temporal denoising** smoothes the displacement list of each vertex, i.e., the displacements along the temporal dimension. It is realized by fitting a cubic penalized regression spline (AlgLib).

Motion Visualization: A real-time capable visualization of the 4D mesh can be obtained using the GPU, or more precisely the OpenGL shader pipeline. Each vertex is uploaded

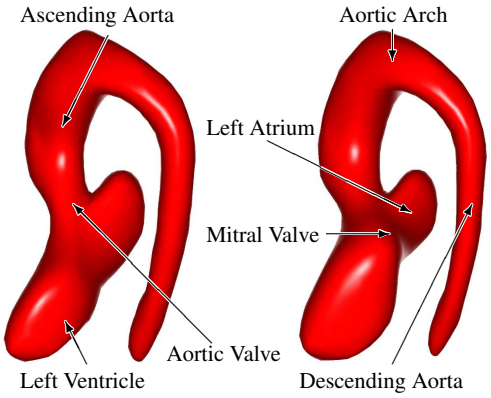

Fig. 6: Cardiac motion visualization. The left ventricle contracts during systole (left) to pump blood into the aorta, resulting in a slightly increased vessel diameter. In the meantime (right), the left atrium fills and then supplies the left ventricle with new oxygenated blood during diastole.

to the GPU with its position, normal and an index to access additional information, which are a list of all triangles, the triangle count per vertex, the corresponding triangle indices, and the displacement list per vertex. A displaced vertex position $\mathbf{v}_t^{\text{dspl}}$ at $t \in \mathbb{R}$ is calculated as linear interpolation between $v_{\lfloor t \rfloor}^{\text{dspl}}$ and $v_{\lceil t \rceil}^{\text{dspl}}$.

A dataset has about 15 temporal positions. Thus, there are 15 displacement vectors in the list. Linear interpolation of these few samples would not lead to a fluent motion visualization. Therefore, ten times as much displacement vectors are resampled from the spline during the temporal denoising. Figure 6 shows a result of the motion visualization.

4.4 Motion-Aware Stroke Volume Quantification

Dynamic Centerlines: The employed Vascular Modeling ToolKit (VMTK) [26] for the centerline extraction [2] requires the specification of a start and an end point on the vessel's surface as input. The user provides these points for the static vessel mesh M to extract the corresponding centerline C. To initialize the extractions of the centerlines C_t for the meshes M_t of each temporal position, the closest points on M_t to the start and end point of C are determined. At this point, M_t does not refer to the independent 3D meshes for each time step (Figure 3e). Instead, M_t is obtained using the postprocessed displacement vectors (Figure 5b, 6).

The dynamic centerline's motion is modeled, obtained, postprocessed and visualized in the same way as the 4D vessel mesh. Solely the projections are performed onto line segments instead of triangles.

Moving Measuring Planes: Measuring planes, orthogonal to the centerline and freely movable along it, are a standard to quantify SVs. To ensure that a plane remains perpendicular to the moving centerline C_t and fits the vessel at

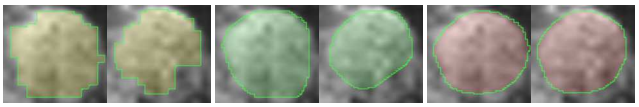

(a) (b) (c)

Fig. 7: Binary mask of the ascending aorta's cross-section for two of 15 temporal positions of the dataset obtained by rasterization of (a) the 4D segmentation, (b) the independent 3D meshes for each time step, (c) the 4D mesh with postprocessed motion information.

every temporal position M_t, the plane's center, normal and scale are modified to a list of size T – analogous to the displacement lists. The centers are derived from the centerline positions and the normals from the tangents. The scales are determined so that the plane fits the diameter of the corresponding vessel section in M_t. Figure 8a shows a measuring plane that fits the vessel at any time and follows the moving centerline, i.e., stays orthogonal.

Stroke Volumes in Dynamic (4D) Vessels: The incorporation of motion into the SV quantification requires an adaption of Equation 1. The check S_3, whether or not a position is inside the vessel, becomes a dynamic counterpart S_4. In addition, planes have a list of T orthonormal systems ($\mathbf{n}^t$, $\mathbf{n}_x^t$, $\mathbf{n}_y^t$), scales $\mathbf{s}^t = \left(s_x^t, s_y^t\right)$ and center positions $\mathbf{c}^t$, $t = 0 \ldots T\text{-}1$. The grid size $\mathbf{g}$ remains constant. Following this, the flow rate calculation $fr(t)$ and transformation to world coordinates $P(x,y,t)$ have to be adjusted to:

$$fr(t) = s_x^t \cdot s_y^t \cdot \mathbf{n}^t \cdot \sum_{x=0}^{g_x\text{-}1} \sum_{y=0}^{g_y\text{-}1} S_4\left(P(x,y,t),t\right) \cdot \mathbb{V}\left(P(x,y,t),t\right)$$

$$\text{with} \quad S_4\left(P(x,y,t),t\right) = \begin{cases} 1, & P(x,y,t) \text{ inside vessel} \\ 0, & \text{else} \end{cases} \tag{2}$$

$$\text{and} \quad P(x,y,t) = \mathbf{c}^t + s_x^t \cdot \left(x - \frac{g_x}{2}\right) \cdot \mathbf{n}_x^t + s_y^t \cdot \left(y - \frac{g_y}{2}\right) \cdot \mathbf{n}_y^t$$

Analogous to the static version, $S_4\left(P(x,y,t),t\right)$ is realized with the dynamic triangular surface, see Figure 7.

5 Results

In this section, we present a validation of the 4D segmentations, an overview of the seven datasets and a discussion. In the implementation, the user is allowed to manually refine the 4D segmentations if desired. However, solely the automatically specified input as described in Section 4 was used for this evaluation. The 4D segmentation including the motion extraction were performed in less than 15 seconds per case on an Intel i7-3930K. The stroke volume (SV) quantifications run in interactive speed. All presented images of vessels and flow were directly captured from our software, which is used for research purposes by the clinical collaborators. Plots were created with MATLAB.

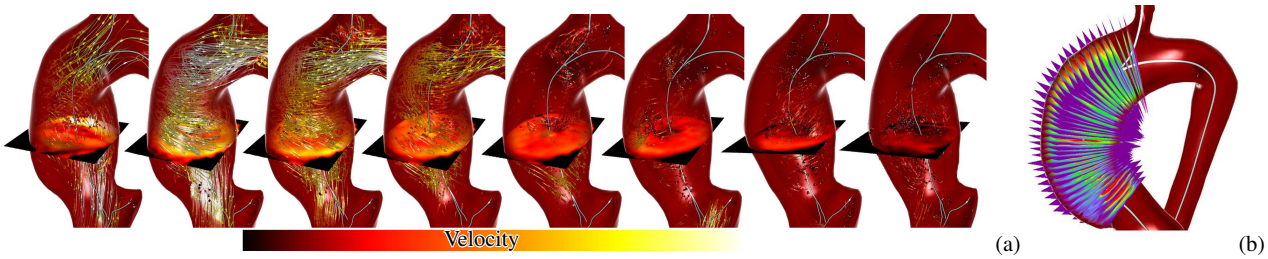

Fig. 8: (a) A measuring plane inside the ascending aorta follows the vessel movement during the cardiac cycle by changing its size and orientation. (b) Equidistant measuring planes in the ascending aorta between the approximate coronary arteries' location and the brachiocephalic artery.

The first vessels that branch off the aorta are the coronary arteries (CAs) directly behind the valve. They receive about 5% of the SV. The next branching vessel is the brachiocephalic artery (BA) in the aortic arch. In order to have a larger range of sample positions to compare the static and motion-aware quantification, we use the constant net flow volume in the ascending aorta after the CAs and before the BA as SV. Figure 8b depicts the evaluated planes in 1 mm steps on the centerline.

5.1 Accuracy of 4D Segmentations

For one dataset (see Figure 8b and 10b), we generated vessel segmentations for all 43 equidistant planes in the ascending aorta manually by drawing contours. Randomly selected samples were validated by the collaborating experts. On the one hand, we performed this on the TMIP of the magnitude images and compared it to the rasterization of the static (3D) vessel surface ("*Static*"). On the other hand, this was done in the anatomical images for each of the 18 temporal positions and compared to the rasterized independent 3D meshes for each temporal position ("*Dyn. (indep.)*") as well as the rasterized dynamic vessel with postprocessed motion information ("*Dynamic*"). Planes were always perpendicular to the vessel's centerline. Each value in Table 1 is an average of all planes. The manual and automatic segmentations overlap by $85.95 \pm 0.62\%$. Cross-sections derived from the static mesh are 10.64% smaller than the manual segmentations. This is the main cause for the 13.65% difference. In the dynamic variant, these sizes differ less. Consequently, large parts of the about 14% discrepancy are caused by the positioning. The 4D mesh with postprocessed motion information directly depends on the independent 3D meshes of each temporal position. Thus, the results of both are similar.

	Static	*Dyn. (indep.)*	*Dynamic*
$(A - M) / M$ (%)	– 10.64	– 4.36	2.44
$(A \cap M) / (A \cup M)$ (%)	86.35	85.23	86.27
$(A \triangle M) / (A \cup M)$ (%)	13.65	14.77	13.73

Table 1: See Figure 9 for a depiction of the areas.

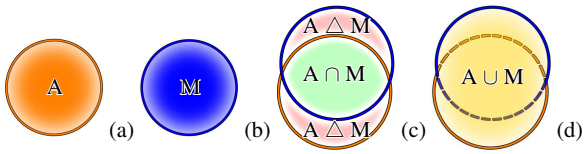

Fig. 9: Cross-section areas that were used to compare the automatic (A) with the manual (M) segmentations.

5.2 Cases

The constant SV between the coronary arteries' location and the brachiocephalic artery was estimated by the collaborating experts for each case and used as a reference. For this purpose, they were allowed to freely move and rotate a measuring plane, obtain multiple SV samples and then estimate a result. In our experiments, the SV was calculated in three different variants "*S*", "*D*" and "*D2*":

- *S* uses the rasterized 3D vessel surface (Figure 2b) that was extracted from the segmentation which is based on the magnitude images' TMIP (recall Equation 1).
- *D* employs the rasterized dynamic (4D) surface with postprocessed motion information from our proposed method (Figures 6, 7c; recall Equation 2).
- *D2* is a simulation of the common 2D PC-MRI. Here, planes are fix (constant angulation, size, center) per centerline position, but the segmentation is time-dependent. The 4D segmentation of the cross-sections is derived from rasterization of the 4D mesh (same as in *D*).

For each variant, the mean of the absolute deviation $\varnothing E_{\{S,D,D2\}}$ per centerline position from the reference was calculated. The plots in Figure 10 show the reference in red, *S* in blue, *D* in green and *D2* in orange. The x-axis shows the centerline positions in 1 mm steps, starting from the approximate coronary arteries' location on the left. *D* performed, on average, 1.57% better than *S* and *D2*. The improvements ranged from -1.0% to 4.12%. *D* was best in four cases, *S* in two and *D2* in one.

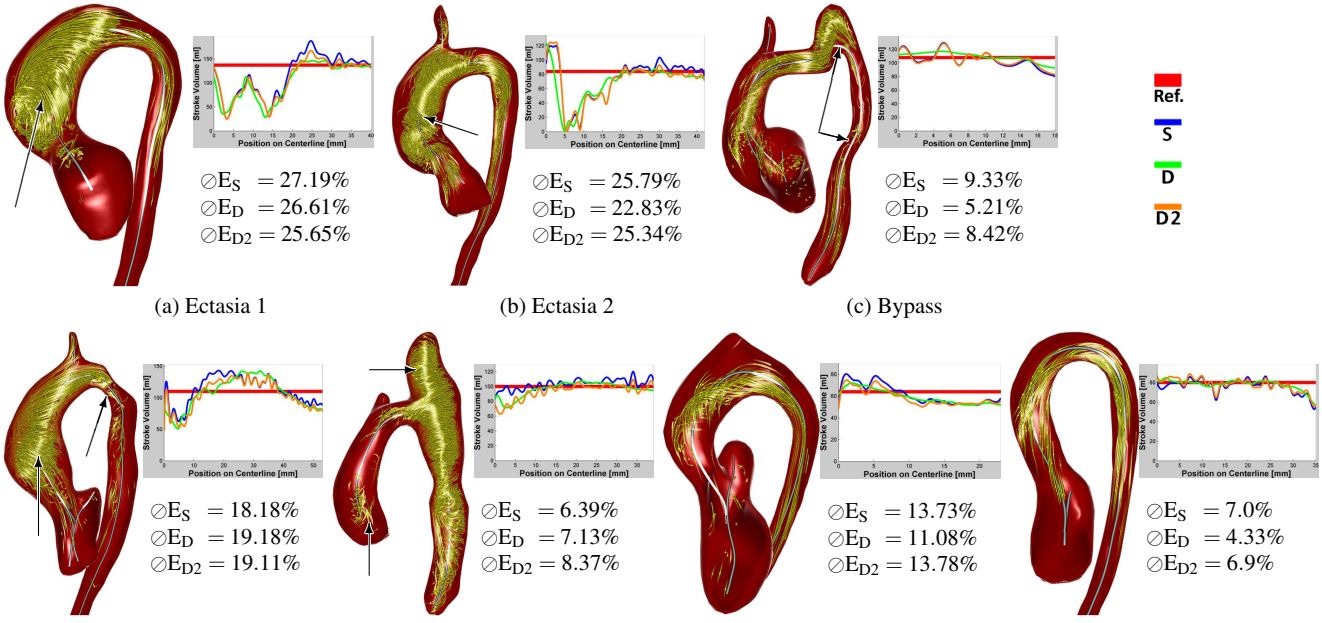

(a) Ectasia 1 (b) Ectasia 2 (c) Bypass

(d) AneuCo (e) AneuBAV (f) Fallot (g) Healthy V.

Fig. 10: Dataset overview with internal vortex flow. The arrows mark present pathologies. The diagrams show stroke volumes obtained with the static (*S*, blue) and dynamic approach (*D*, green) as well as the 2D PC-MRI simulation (*D2*, orange). A reference (red), which is constant in the ascending aorta, was estimated by the collaborating experts. $E_{\{S,D,D2\}}$ is the average percentaged absolute deviation per centerline point of the corresponding method from the reference. (a) Patient with systolic vortex flow in the ectatic ascending aorta. (b) The ectatic ascending aorta of this patient causes systolic vortex flow. (c) A systolic helix in the ascending aorta and aortic arch is promoted by the altered vessel shape of this bypass patient. (d) Systolic vortex flow in the ascending aorta of this patient with an aneurysm and coarctation. (e) Vortex flow after the aortic arch that is present during the whole cardiac cycle. A small systolic vortex in the ascending aorta is a result of the special opening characteristics of the patient's bicuspid aortic valve. (f, g) Physiological helix in the aortic arch during systole in this tetralogy of Fallot patient (f) and healthy volunteer (g).

Ectasia 1: The first patient has a pathologically dilated ascending aorta. Figure 10a shows emerging vortex flow during systole. All SV quantifications are most error-prone in the first half of the examined vessel section, where the vortex is most prominent. The 2D PC-MRI simulation *D2* performs marginally better than *S* and *D* with $\oslash E_{D2} = 25.65\%$.

Ectasia 2: In addition to an ectatic ascending aorta, the second patient has an improperly closing aortic valve which causes an abnormal amount of blood swirling back into the left ventricle during diastole. Figure 10b shows the systolic vortex flow. The diagram depicts the 2.96% improvement of *D* compared to *S*. Like in the previous patient, the heavy vortex flow causes high quantification uncertainties in the first half of the examined vessel section.

Bypass: Extraanatomic bypass surgery was performed in this patient due to a severe coarctation. The motion extraction shows plausible results: there is a strong movement in the aortic root, no noticeable contraction in the vascular replacement and then again a pulsating wall motion. The altered vessel shape promotes systolic vortex flow in the ascending aorta, shown in Figure 10c. Dynamic quantification (*D*) is, on average, 4.12% closer to the reference SV than *S*.

Aneurysm and Coarctation (AneuCo): This patient has an aneurysm in the ascending aorta and a coarctation. As illustrated in Figure 8a, there is a heavy movement in the ascending aorta that causes a high variation of the plane angulation. *S* performs slightly better (0.93%) than the dynamic counterparts, shown in Figure 10d. However, the SV quantification seems to be uncertain due to the present vortex flow.

Aneurysm and BAV (AneuBAV): High velocity blood flow passes this patient's aortic arch and impinges on the wall. A huge vortex emerges that is present during the whole cardiac cycle, shown in Figure 10e. Progression for years probably caused the significant dilation of the left subclavian artery. The patient's bicuspid aortic valve is likely responsible for a smaller systolic vortex in the ascending aorta. The resulting plot illustrates the 0.74% and 1.98% worse performance of *D* and *D2* compared to *S*, respectively.

Fallot: This patient has a pulmonary valve defect as consequence of a surgical tetralogy of Fallot correction. The aorta, however, is free of abnormal flow patterns – only a physiological systolic helix in the aortic arch occurs, as shown in Figure 10f. All quantifications achieve similar results. Yet, D with $\oslash \mathrm{E_D} = 11.08\%$ is, on average, 2.7% closer to the reference than the others.

Healthy Volunteer: The last dataset is from a healthy volunteer with a slight physiological helix in the aortic arch during systole (Figure 10g). All SV curves match the reference relatively well. Yet, with $\oslash \mathrm{E_D} = 4.33\%$, D performs about 2.7% better than the rest.

5.3 Influences

We analyzed influences on the result deviations by correlating the standard deviation (std) of the three obtained SVs from S, D and $D2$ per centerline position i to measures that describe differences between the static and dynamic vessels or measuring planes:

- $\Delta Area$ is the std of minimum and maximum plane areas A^i_S, A^i_D and A^i_D2.
- $\Delta Normal$ refers to angulation changes of measuring planes in D. It is calculated as mean of angles between the average plane normal vector $\oslash\mathbf{n}^i$ and the time-varying plane angulations $\mathbf{n}^i_t$.
- $\Delta Center$ is the mean distance of the time-dependent dynamic measuring plane centers $\mathbf{c}^i_t$ in D from the average plane center $\oslash\mathbf{c}^i$.
- $\Delta Velocity$ is the std of average velocities $||\oslash\mathbf{u}^i_\mathrm{S}||$, $||\oslash\mathbf{u}^i_\mathrm{D}||$ and $||\oslash\mathbf{u}^i_\mathrm{D2}||$ that were sampled on the corresponding planes in S, D and $D2$.

Table 2 shows **no** ($\rho < 0.25$), **low** ($0.25 \leq \rho < 0.5$), **medium** ($0.5 \leq \rho < 0.75$) and **high** ($0.75 \leq \rho$) Pearson correlation coefficients. The normal ($\Delta Normal$) and plane center variation ($\Delta Center$) are the highest influence on deviations of the resulting SVs. Three high and five medium correlations were found in the datasets for these two measures. This seems plausible because both indicate a strong movement of the vessel or, more precisely, the centerline. The sampled average velocities ($\Delta Velocity$) in the cross-sections are the direct consequence of the resulting different plane configurations and rank third. The differences of the measuring plane sizes ($\Delta Area$) rank fourth. An interpretation could be that there is only a moderate amount of vessel pulsation in many cases. Exclusively no or low correlations were detected in the *Ectasia 1* patient. This might indicate that there are other, more complex influences or simply that the differences between the three SVs are not distinctive enough.

Measure \ Dataset	Ectasia 1	Ectasia 2	Bypass	AneuCo	AneuBAV	Fallot	Healthy V.	**Average**
$\Delta Area$	0.19	0.16	0.24	0.14	0.3	0.69	0.64	0.4
$\Delta Normal$	0.43	0.02	0.63	0.5	0.84	0.18	0.53	0.45
$\Delta Center$	0.03	0.74	0.08	0.77	0.56	0.94	0.22	0.48
$\Delta Velocity$	0.23	0.71	0.03	0.69	0.34	0.96	0.11	0.44

Table 2: Pearson-correlation of different measures to the standard deviation of SVs obtained with S, D and $D2$.

5.4 Discussion

The overall deviations from the reference SV were smallest, if there was no prominent vortex flow (Healthy V., AneuBAV, Bypass, Fallot). This coincides with the findings from Köhler et al. [19]. The differences between the 2D PC-MRI simulation $D2$ and S were, on average, smaller than the differences between S and D – especially if there was just a moderate movement of the dynamic centerline. A possible explanation is as follows: The dynamic aorta has its minimum diameter during diastole. During systole, when the maximum diameter is reached due to the pumped blood, the aorta has approximately the same size as the static vessel approximation. Consequently, the difference between flow rates in S and $D2$ is smallest at this time of the cardiac cycle. The changing diameter causes exclusion of peripheral plane regions from the $D2$ quantification during diastole and during the transition from maximum to minimum vessel diameter. Nevertheless, differences between S and $D2$ remain small because of the low diastolic blood flow velocities with little contribution to the SV. In addition, the aorta usually shows a parabolic velocity profile, i.e. the main blood flow jet with highest influence on the SV calculation is located in the center, as depicted in Figure 11.

Limitations: Contrast in the anatomical images strongly varies due to the pulsatile flow, making the automatic segmentation challenging during diastole. Correcting intensity inhomogeneities [30] might increase the robustness. Divergence-free filters [23] may be applied as further phase image preprocessing. The effect of phase dispersion [35] was not considered, but could introduce errors at the vessel

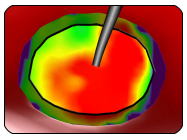

Fig. 11: A plane, color-coded by velocity, orthogonal to the centerline (gray) inside the vessel (red surrounding). Motion-aware stroke volume quantification excludes peripheral regions (darkened) while the vessel diameter is below maximum. Yet, the difference using static vessels is relatively small since high velocities with most influence on the stroke volume quantification are often located in the center.

boundaries. Scans with retrospective gating could produce different results, since early-systolic values are better captured. Generally, image data with a higher spatio-temporal resolution might generate more significant SV differences.

6 Conclusion and Future Work

We have presented a cardiac motion extraction that is feasible for the clinical routine due to minimal required interaction. We focused on the aorta, but the application of our method to other vessels such as the pulmonary artery is possible. Graph cuts were employed to support segmentation tasks and showed a high level of acceptance among the consulted radiologists because of the intuitive task of specifying regions inside and outside the vessel. Such regions were automatically determined for each temporal position and can be used for other segmentation algorithms as well.

We incorporated vessel dynamics to adjust stroke volume calculation and quantified differences to conventional methods using static vessels and a simulation of 2D PC-MRI. On average, the results differed by 7.82%. Unfortunately, the incorporation of motion information does not achieve improvements for each position of the centerline and thus is no guarantee for more accurate results. Yet, it performed on average 1.57% better by having lower differences to the reference stroke volumes estimated by the clinical collaborators. Limitations were pointed out. Variations of the planes' normal vectors and centers had the highest correlations to differences of the SVs obtained with the different methods. This is plausible since both indicate a strong vessel movement. The limited improvements imply that it is reasonable to employ static 3D vessel approximations to quantify stroke volumes. Yet, the use of robust methods [19] is recommended due to the calculations' high sensitivity to the measuring plane angulation.

Outlook: Motion information open up various opportunities. Wall shear stress is another important measure that strongly depends on the accurate wall position and orientation. Possible improvements by incorporating vessel dynamics should be investigated. Models of the aortic valve facilitate further understanding of vortex formation in, e.g., bicuspid aortic valve patients. The extracted movement could support the determination of the valve's exact position and location. Finally, the wall movement allows conclusions regarding vessel elasticity, which is important for the risk assessment of aneurysm rupture and thus supports treatment decisions. The derivation of a vascular wall model was a major interest of the consulted experts.

Further research to assess the reliability of the obtained results is necessary. In the future, standardized and (semi-)automatic evaluation methods will enable the fast processing of large studies that are performed for statistical analysis of gender- and age-specific norm values. The derived physiological variations of different flow parameters will support the assessment of disease severity.

Conflict of Interest Benjamin Köhler, Uta Preim, Matthias Grothoff, Matthias Gutberlet, Katharina Fischbach and Bernhard Preim declare that they have no conflict of interest. Informed consent was obtained from all patients for being included in the study.

References

1. Abufadel, A.: 4D Segmentation of Cardiac MRI Data Using Active Surfaces with Spatiotemporal Shape Priors. Ph.D. thesis, Georgia Institute of Technology (2006)
2. Antiga, L., Iordache, E.B., Remuzzi, A.: Computational Geometry for Patient-Specific Reconstruction and Meshing of Blood Vessels from MR and CT Angiography. IEEE Trans Med Imag **22**(5), 674–84 (2003)
3. Bade, R., Haase, J., Preim, B.: Comparison of Fundamental Mesh Smoothing Algorithms for Medical Surface Models. In: Simulation und Visualisierung, pp. 289–304 (2006)
4. Born, S., Markl, M., Gutberlet, M., Scheuermann, G.: Illustrative Visualization of Cardiac and Aortic Blood Flow from 4D MRI Data. In: Proc IEEE PacificVis, pp. 129–36 (2013)
5. Born, S., Pfeifle, M., Markl, M., Gutberlet, M., Scheuermann, G.: Visual Analysis of Cardiac 4D MRI Blood Flow Using Line Predicates. IEEE Trans Vis Comput Graph **19**, 900–12 (2013)
6. Calkoen, E.E., Roest, A.A., van der Geest, R.J., de Roos, A., Westenberg, J.J.: Cardiovascular Function and Flow by 4-Dimensional Magnetic Resonance Imaging Techniques: New Applications. J Thorac Imag **29**(3), 185–96 (2014)
7. Carnecky, R., Brunner, T., Born, S., Waser, J., Heine, C., Peikert, R.: Vortex Detection in 4D MRI Data: Using the Proper Orthogonal Decomposition for Improved Noise-Robustness. In: EuroVis Short Papers, pp. 127–31 (2014)
8. Cousty, J., Najman, L., Couprie, M., Guinaudeau, S.C., Goissen, T., Garot, J.: Segmentation of 4D Cardiac MRI: Automated Method based on Spatio-Temporal Watershed Cuts. Image Vis Comput **28**(8), 1229–43 (2010)
9. Dìaz, C., Robles, L.A.: Fast Noncontinuous Path Phase-Unwrapping Algorithm based on Gradients and Mask. In: Proc Iberoameric Cong Patt Recog (CIARP), pp. 116–23 (2004)
10. Dormand, J.R., Prince, P.J.: A Family of Embedded Runge-Kutta Formulae. J Comput Appl Math **6**, 19–26 (1980)
11. Francois, C., Srinivasan, S., Schiebler, M., Reeder, S., Niespodzany, E., Landgraf, B., Wieben, O., Frydrychowicz, A.: 4D Cardiovascular Magnetic Resonance Velocity Mapping of Alterations of Right Heart Flow Patterns and Main Pulmonary Artery Hemodynamics in Tetralogy of Fallot. J Cardiovasc Magn Reson **14**(1), 16 (2012)
12. Gasteiger, R., Neugebauer, M., Beuing, O., Preim, B.: The FLOWLENS: A Focus-and-Context Visualization Approach for Exploration of Blood Flow in Cerebral Aneurysms. IEEE Trans Vis Comput Graph **17**(12), 2183–92 (2011)
13. Gasteiger, R., Neugebauer, M., Kubisch, C., Preim, B.: Adapted Surface Visualization of Cerebral Aneurysms with Embedded Blood Flow Information. In: Proc Eurographics Vis Comput Biol Med, pp. 25–32 (2010)
14. Hennemuth, A., Friman, O., Schumann, C., Bock, J., Drexl, J., Huellebrand, M., Markl, M., Peitgen, H.O.: Fast Interactive Exploration of 4D MRI Flow Data. Proc Int Soc Opt Phot (SPIE) **7964** (2011)
15. Hope, M.D., Sedlic, T., Dyverfeldt, P.: Cardiothoracic Magnetic Resonance Flow Imaging. J Thorac Imag **28**(4), 217–30 (2013)
16. Hope, M.D., Wrenn, J., Sigovan, M., Foster, E., Tseng, E.E., Saloner, D.: Imaging Biomarkers of Aortic Disease - Increased Growth Rates with Eccentric Systolic Flow. J Amer Coll Cardiol **60**(4), 356–7 (2012)

17. Hoppe, H.: New Quadric Metric for Simplifying Meshes with Appearance Attributes. In: Proc IEEE Vis, pp. 59–66 (1999)
18. Köhler, B., Gasteiger, R., Preim, U., Theisel, H., Gutberlet, M., Preim, B.: Semi-Automatic Vortex Extraction in 4D PC-MRI Cardiac Blood Flow Data Using Line Predicates. IEEE Trans Vis Comput Graph **19**(12), 2773–82 (2013)
19. Köhler, B., Preim, U., Grothoff, M., Gutberlet, M., Fischbach, K., Preim, B.: Robust Cardiac Function Assessment in 4D PC-MRI Data of the Aorta and Pulmonary Artery. Comp Graph Forum (to appear) (2015)
20. Lombaert, H., Sun, Y., Cheriet, F.: Fast 4D Segmentation of Large Datasets Using Graph Cuts. In: Proc Int Soc Opt Phot (SPIE), pp. 79,622H–79,622H–7 (2011)
21. Mahapatra, M., Buhmann, J.M.: Automatic Cardiac RV Segmentation Using Semantic Information with Graph Cuts. In: Proc Int Symp Biomed Imag, pp. 1106–9 (2013)
22. McLoughlin, T., Laramee, R.S., Peikert, R., Post, F.H., Chen, M.: Over Two Decades of Integration-Based, Geometric Flow. Comp Graph Forum **29**(6), 1807–29 (2010)
23. Ong, F., Uecker, M., Tariq, U., Hsiao, A., Alley, M.T., Vasanawala, S.S., Lustig, M.: Robust 4D Flow Denoising Using Divergence-free Wavelet Transform. J Magn Reson Med **73**(2), 828–42 (2015)
24. van Ooij, P., Potters, W.V., Guédon, A., Schneiders, J.J., Marquering, H.A., Majoie, C.B., Vanbavel, E., Nederveen, A.J.: Wall Shear Stress Estimated with Phase Contrast MRI in an In Vitro and In Vivo Intracranial Aneurysm. J Magn Reson Imag **38**(4), 876–84 (2013)
25. van Pelt, R., Bescos, J.O., Breeuwer, M., Rachel, E.C., Gröller, M.E., ter Haar Romenij, B., Vilanova, A.: Exploration of 4D MRI Blood Flow Using Stylistic Visualization. IEEE Trans Vis Comput Graph **16**(6), 1339–47 (2010)
26. Piccinelli, M., Veneziani, A., Steinman, D.A., Remuzzi, A., Antiga, L.: A Framework for Geometric Analysis of Vascular Structures: Application to Cerebral Aneurysms. IEEE Trans Med Imag **28**(8), 1141–55 (2009)
27. Potters, W.V., Cibis, M., Marquering, H.A., van Bavel, E., Gijsen, F., Wentzel, J.J., Nederveen, A.J.: 4D MRI-Based Wall Shear Stress Quantification in the Carotid Bifurcation: A Validation Study in Volunteers Using Computational Fluid Dynamics. J Cardiovasc Magn Reson **16**(Suppl 1), P162 (2014)
28. Preim, B., Botha, C.: Visual Computing for Medicine, 2 edn. Morgan Kaufmann Publishers (2013)
29. Roldán-Alzate, A., Frydrychowicz, A., Johnson, K.M., Kellihan, H., Chesler, N.C., Wieben, O., Francois, C.J.: Non-invasive Assessment of Cardiac Function and Pulmonary Vascular Resistance in an Canine Model of Acute Thromboembolic Pulmonary Hypertension Using 4D Flow Cardiovascular Magnetic Resonance. J Cardiovasc Magn Reson **16**(1), 23 (2014)
30. Salvado, O., Hillenbrand, C., Zhang, S., Wilson, D.L.: Method to Correct Intensity Inhomogeneity in MR Images for Atherosclerosis Characterization. IEEE Trans Med Imag **25**(5), 539–52 (2006)
31. Stankovic, Z., Allen, B.D., Garcia, J., Jarvis, K.B., Markl, M.: 4D Flow Imaging With MRI. Cardiovasc Diagn Ther **4**(2), 173–92 (2014)
32. Taubin, G., Zhang, T., Golub, G.: Optimal Surface Smoothing as Filter Design. In: Proc Europ Conf Comput Vis, pp. 283–92 (1996)
33. Venkataraman, S.: 4D Visualization of Cardiac Flow (2010). NVIDIA GPU Tech Conf Talk
34. Walker, P.G., Cranney, G.B., Scheidegger, M.B., Waseleski, G., Pohost, G.M., Yoganathan, A.P.: Semiautomated Method for Noise Reduction and Background Phase Error Correction in MR Phase Velocity Data. J Magn Reson Imag **3**(3), 521–30 (1993)
35. Wolf, R.L., Ehman, R.L., Riederer, S.J., Rossman, P.J.: Analysis of Systematic and Random Error in MR Volumetric Flow Measurements. J Magn Reson Med **30**(1), 82–91 (1993)
36. Zhang, Q., Eagleson, R., Peters, T.M.: Dynamic Real-Time 4D Cardiac MDCT Image Display Using GPU-Accelerated Volume Rendering. Comp Med Imag Graph **33**(6), 461–76 (2009)
37. Zhao, F., Zhang, H., Wahle, A., Scholz, T.D., Sonka, M.: Automated 4D Segmentation of Aortic Magnetic Resonance Images. In: Proc Brit Mach Vis Conf, pp. 247–56 (2006)